Fabrication of Translucent Graded Dental Crown Using Zirconia-Yttrium Multi-Slurry Tape Casting 3D Printer

Mr. Yulius Shan Romario, Ph.D. student
Graduate Institute of Manufacturing Technology, National Taipei University of Technology, Taipei, Taiwan
1, Sec. 3, Zhongxiao E. Rd., Taipei, 10608 Taiwan
Email: yulius.romario@gmail.com

Dr. Chinmai Bhat, Ph.D.
Research Assistant, High-value Biomaterials Research and Commercialization Center, National Taipei University of Technology, Taipei, Taiwan
1, Sec. 3, Zhongxiao E. Rd., Taipei, 10608 Taiwan
Email: cvbhatjkd@gmail.com

Dr. Maziar Ramezani, Ph.D.
Professor,Department of Mechanical Engineering, Auckland University of Technology, Auckland 1010, New Zealand
Email: maziar.ramezani@aut.ac.nz

Dr.Tim Pasang, Ph.D.
Professor, Department of Engineering Design, Manufacturing and Management Systems, Western Michigan University, Kalamazoo MI 4900-5200 USA
Email: tim.pasang@wmich.edu

Dr. Zhangwei Chen, Ph.D.*
Professor, Additive Manufacturing Institute, Shenzhen University, Shenzhen, 518060, China
Guangdong Key Laboratory of Electromagnetic Control and Intelligent Robotics, College of Mechatronics and Control Engineering, Shenzhen University, Shenzhen, 518060, China
Email: chen@szu.edu.cn

Dr. Cho-Pei Jiang, Ph.D.*
Professor, Department of Mechanical Engineering, National Taipei University of Technology, Taiwan
1, Sec. 3, Zhongxiao E. Rd., Taipei, 10608 Taiwan
Email: jcp@mail.ntut.edu.tw

Corresponding Author: jcp@mail.ntut.edu.tw, chen@szu.edu.cn

Abstract

This paper aims to fabricate functionally graded dental crown using a multi-slurry tape casting additive manufacturing technology. The different luminescence of the dental crown was obtained with different composition of zirconia and yttria. Zirconia with tunable mechanical properties and translucency are obtained by adding 3, 3.5, 4, 4.5, and 5 mol% of yttrium oxide to zirconia powder. After obtaining the printable slurry with maximum solid loading, the green bodies are prepared using the in-house built high speed multi-ceramic tape casting technology. They are later sintered with two-stage sintering method. After the successful fabrication, the mechanical properties and translucency of the specimens were evaluated with Vickers hardness, three-point bending and translucency parameter tests. Finally, an FGM tooth crown with five photocurable slurries is proposed to demonstrate the translucent gradient effect of sintered part. The solid loading of 80% zirconia and 20% resin delivered samples without any surface cracks. The shrinkage ratio analysis showed that the sintered sample dimension was reduced by 20%, 20%, and 23% along X, Y, and Z directions. The samples fabricated with 3% yttrium oxide to zirconia delivered excellent hardness (1687 HV) and flexural strength (650.6 MPa). However, the relative luminescence increased with increasing the yttrium oxide for 3 – 5 mol%. With the optimized process parameters, the proposed dental crown is fabricated and analyzed for their shrinkage ratio, mechanical, and translucency properties. The study proposes the potential of fabricating customized dental crown with gradient translucent appearance.

***Keywords:** Functionally graded materials, multi-slurry tape casting 3D printing, vat photopolymerization, dental crown, translucency*

Introduction

The demand for components with function of specific properties are exponentially increasing in various industries such as aerospace, automobile, medical, and defense industries [1]. The term function is defined as the response of the structures to its external stimulus (i.e. load). The components that are capable of tuning the responses i.e. varying the properties depending on the load is much needed for various mobility and electronic components [2, 3].

Figure 1a shows the major fields where functionally graded materials (FGMs) are extensively used [4]. In this regard, researchers worldwide are developing various kinds of FGM that can be pre-set with different structural and mechanical properties at different positions in the material [5-7]. With the FGMs, various properties such as hardness, toughness, wear, corrosion and resistance can be attained in a single component, without losing their constitutive material properties [8]. Different FGMs developed so far can be broadly classified into continuous and discrete graded materials [9]. In a continuous gradient material, variation in material composition or microstructure occurs continuously along the depth. On the other hand, in discrete gradient materials, the microstructure is characterized by a stepwise change which results in a multilayer structure with an interface between discrete layers. Figure 1b shows the worldwide advancement in the FGMs based on the number of publications by various research institutions and organizations.

Conventional manufacturing techniques of FGMs include powder metallurgy [10], centrifugal casting method [11], centrifugal slurry method [12], centrifugal mixed-powder [9], laser cladding [13], vapor deposition processing [14], and plasma spray forming [15]. Powder metallurgy technique is widely used to fabricate various kinds of

FGMs. However, inhomogeneous powder consolidation and linear grading are some of the major drawbacks posed by this technique [16]. Furthermore, the major disadvantage associated with conventional manufacturing technique include its inability to fabricate complex structures without joints. Apart from that, the conventional manufacturing techniques cannot fulfill the growing requirements of high-mass specific lattice structures due to various manufacturing constraints [17]. Moreover, the current conventional technique only focusses on the fabrication of FGMs with grading in the linear direction [16]. Customized-grading is not possible due to complexity of the processes and constraints involved.

The recent development in the additive manufacturing has enabled in the development of complex shaped FGMs that can be customized as per the user's requirements. The FGMs can be coupled with complex lattice structures to deliver high mass specific properties. Moreover, additive manufacturing technologies further reduce the processing step, thereby fabricating complex FGMs with minimum cost and maximum accuracy [18-20].

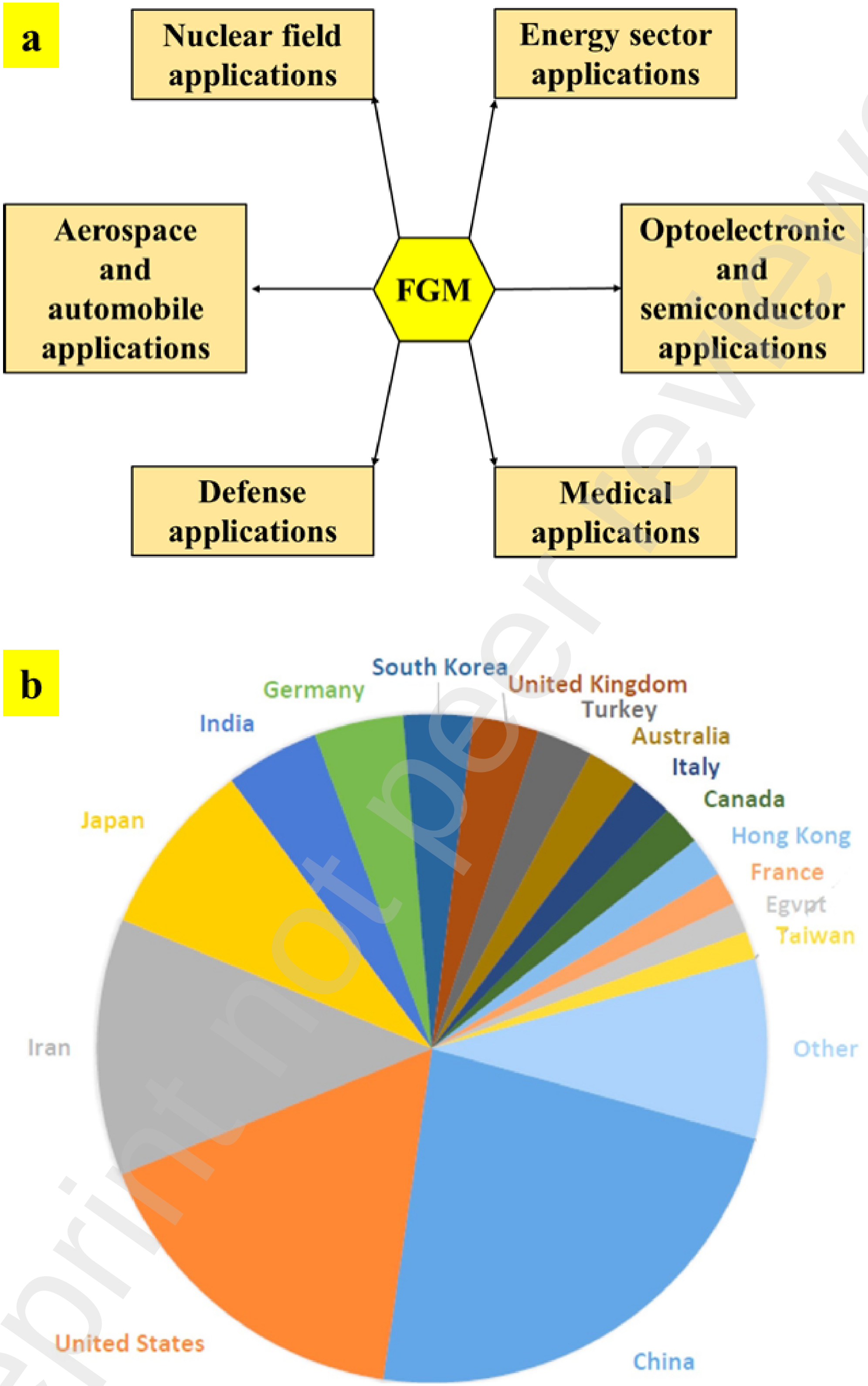

Figure 1: Advancement in the functionally graded materials (FGMs): a) Major field where FGMs are widely used and b) Country-wise publications on FGMs [4].

Some of the researchers worldwide has developed FGMs using various additive manufacturing technologies [21]. Of the various methods, multi-material extrusion processing is the most commonly used method [22]. A frozen-form triple-extruder additive manufacturing (AM) technique was applied to print discrete functionally graded components composed of alumina and zirconia [23]. This printing process needs to be performed in a closed and refrigerated environment because of water being used as binder. Another study used a multi-nozzle extrusion printer to fabricate the ceramic-based discrete FGM component with different compositions of ceramic filaments [22]. The fabricated component experienced delamination after the sintering due to differential shrinkage rates of ceramic filaments being used. The success rate of printing ceramic FGM components green bodies by material extrusion process is high and is also economic. However, the occurrence of delamination post sintering is frequently observed and seldom addressed. This drawback can be reduced by optimization of the heating rate for the sintering process but the printable size is limited [24].

Vat photopolymerization (VPP) process, consisting of bottom-up and top-down methods, is an alternative method for making ceramic discrete FGM components. A two-vat based VPP process involving bottom-up technique successfully printed the FGM component [25]. The disadvantage is that the volumetric alumina powder content of the slurry is low, and only two vats was used resulting in fabrication limitation of two-stepwise discrete FGM component. A three-stepwise FGM components was printed successfully using a multi-slurry VPP technology using a manipulator (to switch the material) to deposit and pave the slurry layer with different proportions of Si_3N_4 and Al_2O_3 slurries [26]. All these VPP based additive manufacturing technologies used bottom-up approach in fabricating ceramic based FGMs. However, controlling the composition and their deposition is a challenging task using this approach [27]. The limitations on the number of discrete layers that can be achieved using this approach make it a lesser preferable choice. Top-down method is an alternative approach that can print more discrete homogenous layers of FGM components [28]. This method can deposit different slurries on the platform using an extrusion head. However, the disadvantage of the top-down method is that the cured FGM green body is located inside the built block composed of different slurries, making it impossible to be recycled and reused after it is removed from the platform by solvents [29]. Therefore, reducing the wastage of slurry in the FGM green body printing becomes a key issue for VPP 3D printers based on a top-down method.

Tape-casting slurry 3D printer is an innovative method of VPP based top-down method that uses a tape on which slurry can be poured and paved rather than vat [30]. The thin layer of slurry can be extruded on the tape and paved using a paving system. The unsolidified slurry can be shoveled and recycled for reuse. This saves a lot of material during printing along with effectively fabricating functionally graded materials. Another advantage of this process is that it can deposit different slurries on a tape for multi-slurry 3D printing.

Zhang et al. developed the tape casting technology for the fabrication of illite [31]. The study successfully fabricated the lattice structures using the illite material which could not be processed by any other AM process. A similar study was also carried out by Rosenberger et al. to fabricate the alumina inks made up of Al_2O_3 powders and platelets [32]. Though these studies focused on developing the tape casting technology for a single material, Xing et al. developed the multi-ceramic tape casting for the first time [33]. The functionally graded Al_2O_3-Si_3N_4 material was fabricated with different weight percentage of both materials using the manipulator system. Though this study successfully demonstrated the possibility of multi-ceramic tape casting, it lacked the speed as it utilized the point-based UV laser system. In the current study, the DLP based high-speed multi-ceramic tape casting technology is developed which can fabricate the 2D layer at a time, thereby faster fabrication of complex structures.

The aim of this study is to propose a multi-slurry tape-casting 3D printing technology for printing the transparent gradient zirconia material. The construction of the printer is explained in detail along with its working demonstration. Functionally graded zirconia is printed with this technology. The composition of zirconia is varied along the linear direction with the addition of yttrium oxide powder (Y_2O_3). Five types of zirconia powders with different yttrium oxide powder content are prepared to synthesize the photocurable slurries. Printing parameters are optimized to print the green body of specimen. A two-stage sintering process is adopted to crystalize the printed part. Mechanical and optical properties of sintered parts are evaluated for benchmarking. To demonstrate the potential application of this technology, a dental crown is fabricated which replicates the exact appearance of human tooth. So far, the additive manufacturing of dental crown used fixed transparency ceramic tooth [34-36]. However, with this technology, tooth with gradient transparency can be fabricated with opaque root part and gradual variation of brightness along the crown part. Such a variation in transparency can be brought in by varying the composition of yttrium oxide.

Though the current study mainly focuses on the fabrication of a tooth as a demonstration, several other applications can be explored using this newly developed technology. With several upgradations, this technology can be utilized in the fabrication of turbine blades with varying thermal conductivity materials, bone scaffolds with varying calcium contents, etc. This technology has potential to deliver several economic engineering solutions with tunable functional properties.

2. Method and materials

2-1. High speed multi-slurry tape-casting process

In the current study, special focus was given to the development of photopolymerization based additive manufacturing process that is economic, yet, capable of fabricating functionally graded materials with high accuracy. The printing ability of newly developed machine is demonstrated with different graded zirconia material. Nevertheless, the machine is also capable of printing multi-materials where different resins can be used in different vats. Figure 2a schematically represents the working principle of the multi-slurry tape-casting 3D printing process. Compared to the conventional vat-photopolymerization process, the resin containing vat is replaced by an optical transparent sheet. The slurry which has higher viscosity compared to that of vat, is extruded through the nozzle. The extruded slurry is dropped on the transparent sheet which is then paved with a scraper to obtain a thin and flat surface of slurry. The single extruder nozzle can be connected to the multiple slurry tanks with different composition. In this study, five different types of slurry can be on-demand deposited on the transparent sheet through a switching device. The g-code is designed in such a manner to control the switching and lower the build platform by one layer thickness. Thus, the 3D green body with multiple slurries can be printed layer-by-layer. Figure 2b shows the construction of 3D printer. The ultrasonic cleaner shown in Figure 2b is used to clean each layer after being printed to prevent contamination. The Z-axis is programmed to rotate 90º after successful printing of each layer to facilitate cleaning.

A liquid crystal displayer (LCD) panel under the printing area is set up to generate the pattern of each layer. The LCD panel consists of an array of LED array, that can emit 160 Watt of energy through to project the image of the layer onto the transparent sheet. The wavelength of the beam used in this study is 405 nm. Upon exposure, the slurry on the transparent sheet undergoes photopolymerization and solidification. The platform lifts up after each layer being printed. There is almost no adhesive force between the sheet and the materials due to excellent flexibility of the transparent sheet. The transparent sheet that has been coated with on-demand slurry moves forward to the printing area, and the platform descends for exposure and curing (Figure 2a). The above procedure is repeated until the printing is completed.

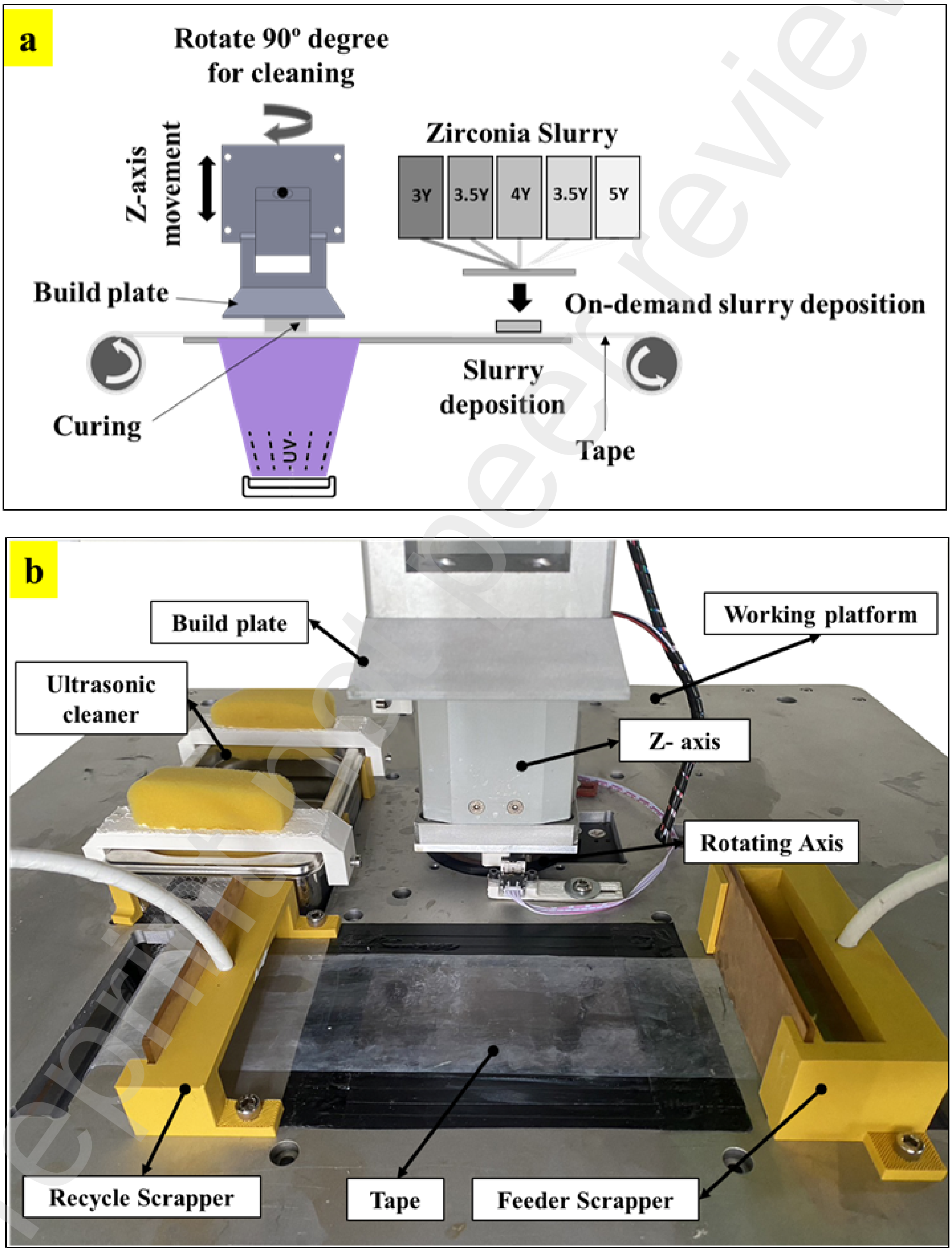

Figure 2: Multi-slurry tape-casting 3D printing: (a) working principle (b) components

of the 3D printer

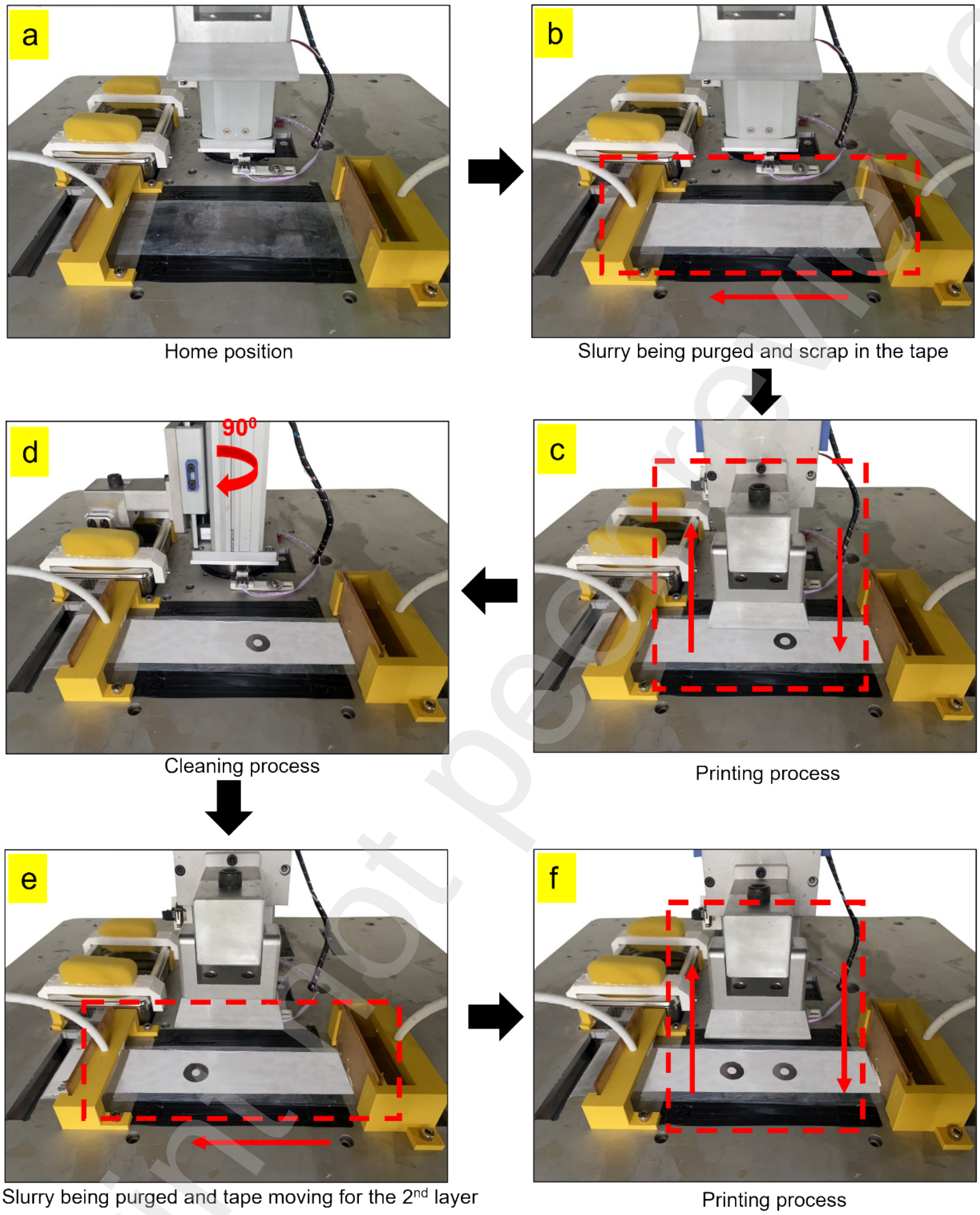

Figure 3: Working demonstration of multi-slurry tape-casting 3D printer (a) home position (b) scrapping process (c) printing process (d) cleaning process (e) tape moving for the next layer (f) printing process

The working of the 3D printer is demonstrated in Figure 3. Figure 3a corresponds to the printer at home position. The printing process begins from this position. In Figure

3b, the slurry is being purged on the tape using the feeder scrapper and spread to the thin layer across the tape. Once the slurry is evenly spread across the tape, printing process begins as shown in Figure 3c. During the printing, the build plate moves down and touches the slurry. The LCD display unit will emit the radiation corresponding to the slicer profile to cure the single two-dimensional layer. Once, the single layer is completely cured, the build plate lifts up as shown in the Figure 3c. The absence of slurry over the tape in Figure 3c can be traced on the build plate in its cured state. Following the printing, the Z-axis rotates to an angle of 90° to clean the printed layer using ultrasonic cleaner (Figure 3d). Such cleaning process after every layer would prevent contamination, thereby enhancing the cohesion between successive layers. Figure 3e shows that the build plated is rotated to an angle of -90° (i.e. to its initial position) to repeat printing. The printing process repeats as explained earlier until the whole sample/specimen is printed. Figure 3f shows the printing of 2nd layer (the absence of slurry represents that the corresponding amount of slurry is printed on the build plate and cured).

2-2. Slurry preparation

The photocurable resin is prepared using low-viscosity HDDA (1,6-Hexanediol diacrylate, UM82-030, Evermore Chemical Industry Co. Taiwan) resin and 1 wt.% of photo-initiator (2,4,6-trimethylbenzoyldiphenyl phosphine oxide, Doublecure TPO, Double bond Chemical Co., Taiwan).

Five different compositions of zirconia powders: 3Y-TZP, 3.5Y- TZP, 4Y-TZP, 4.5Y- TZP and 5Y-TZP (ZrO_2, Zipro Technology, Taipei, Taiwan) are prepared, consisting of tetragonal zirconia mixed with 3, 3.5, 4, 4.5 and 5 mol.% of Y_2O_3, respectively.

The zirconia powder is added to the photocurable resin to form a photocurable slurry. Since the percentage of zirconia powder will affects the curing efficiency and shrinkage rate, the solid loading percentage (vol.%) of the zirconia powder is used as a variable in this study. The maximum zirconia powder content that can be successfully printed with the developed 3D printer is considered for the further studies. Therefore, the content of the zirconia powder in the photocurable resin is 50, 60, 70 and 80 wt.%, respectively. Table 1 shows the composition of slurry.

Table 1. Composition of the zirconia slurry

Composition	Zirconia		HDDA		TPO	
	(wt%)	(vol.%)	(wt%)	(vol.%)	(wt%)	(vol.%)
50/50	50.00	14.64	49.00	83.82	1.00	1.54
60/40	60.00	20.47	39.00	77.73	1.00	1.80
70/30	70.00	28.61	29.00	69.24	1.00	2.15
80/20	80.00	40.77	19.00	56.55	1.00	2.68

2-3. Viscosity

The level of flatness of the purged slurry on the cast tape depends on the coefficient of viscosity of the slurry. Thus, the slurry should be prepared with appropriate coefficient of viscosity to obtain excellent print quality. In this study, the coefficient of viscosity of the slurry was measured at room temperature using a viscosity tester (Brookfield DV3T, Ametek, Massachusetts, United Kingdom).

2-4. Curing property

The solid loading of the powder in the photocurable slurry is one of the factors affecting the curing depth. Thus, the relationship between the curing depth and the light energy absorbed by the photocurable slurry is not linear. The exposure time is regarded as an indicator of the exposure energy for the photocurable slurry due to the power intensity of the LED array is fixed. Therefore, experiments with different exposure times were carried out for these four slurries with different solid loadings. The main goal of this test is to analyze the relationship between exposure time and curing depth after obtaining the highest solid loading of the printable photocurable slurry.

2-5 Sintering treatment for printed green body

The sintering process is carried out in two stages. In the first stage, the sintering temperature is utilized to vaporize the solidified photocurable resin. Thus, the green body after the first stage of sintering essentially contains only zirconia powder. The second stage of sintering is subsequently carried out at higher temperature to fuse the ceramic particles.

In this study, the thermogravimetric analysis (TGA) was used to determine the temperature corresponding to vaporization of solidified resin (i.e. first stage sintering temperature). The subsequent sintering involves zirconia whose sintering temperature is readily available in literature. The common sintering temperatures for zirconia lie in the range of 1400-1600 °C. Moreover, it is reported that the T-phase zirconia can be obtained at the sintering temperature of 1550°C [37]. Thus, 1550°C was adopted as the second stage sintering temperature in this study.

2-6. Shrinkage ratio

In the first stage of sintering, the photopolymerized resin in the printed green body is vaporized which leads to initial volume shrinkage. The powder is then fused to produce crystals at the second-stage sintering temperature resulting in secondary volume reduction (i.e. shrinkage). Thus, the shrinkage ratio has to be analyzed to evaluate the difference in dimension. This difference in dimension has to added in excess to the CAD design (green body) as a shrinkage allowance. Five specimens of the dimension $10\times15\times5$ mm^3 is printed with each slurry type (composition). The dimension of the green body and the sintered part is determined to evaluate the shrinkage ratio of each part. Furthermore, the results obtained from this study would also analyze the effect of composition on the percentage of shrinkage.

2-7. Measurement of mechanical properties

Evaluating the mechanical properties of the printed samples is very important to shows the efficacy of the newly developed printer. Furthermore, the mechanical properties of samples fabricated with this technique can also be benchmarked, which can be used in future for comparison. The mechanical properties are measured using hardness and flexural strength analyzing techniques as listed below:

2-7-1. Hardness

Vickers hardness test (HMV-2000, Shimadzu, Japan) is used to measure the surface hardness of each specimen. The hardness of each specimen is evaluated by analyzing Vickers's hardness number at six different locations and averaging them.

2-7-2. Flexural strength

The flexural strength of the sintered specimen can be obtained using three-point bending test (Universal Testing Machine CY-20, Chun-Yen Co., Taiwan). Six pieces of sintered specimen with a dimension of 2 mm × 1.5 mm × 25 mm are prepared. The span length is set to 20 mm according to the ASTM C161-13. The pressure probe moves down at a speed of 0.1mm/min until the test bar breaks. The flexural strength is then evaluated by the maximum load recorded by the probe.

2-8. Application of multi-slurry tape-casting technology

Dental crown is one such field where this technology can be of immense applications. The translucent appearance of tooth gradually varies from opaque root to the glowing tip. The current dental crown fabricated by additive manufacturing technique cannot imitate the appearance of real tooth. Hence, it is easily identifiable. With the functionally gradient materials that can be obtained with this newly developed technology, it is now possible to obtain translucent gradient appearance. The Y_2O_3 material added to the zirconia powder increases luminescence. Thus, the composition of Y_2O_3 and zirconia powder can be controlled to control the luminescent gradient.

Incisor tooth is an application of printing FGM with translucence gradient because it is gradually translucence from the opaque root to the tip. Figure 4 shows the CAD design of incisor tooth model with hollow features, which has a dimension 9.44 × 8.34 × 10.73 mm. The hollow features are provided for necessary implanting. The translucent gradient is demonstrated with a five-stepwise model with 3Y at the root and 5Y at the tip as shown in Figure 5.

2-8-1. Translucency parameter

The relative luminance is adopted to obtain the value of the translucency parameter (TP). Each point in the color space is normalized to 0 for the darkest black and 1 for the lightest white [38]. The relative luminance of a color is evaluated as per the Equations 1 - 4:

$$L : 0.2126 \times R + 0.7152 \times G + 0.0722 \times B \tag{1}$$

where R, G, B values can be obtained by the following equations:

$$\text{if } RsRGB \leq 0.03928 \text{ then } R = \frac{RsRGB}{12.92} \text{ else } R = \left(\frac{RsRGB + 0.055}{1.055}\right)^{2.4} \tag{2}$$

$$\text{if } GsRGB \leq 0.03928 \text{ then } G = \frac{GsRGB}{12.92} \text{ else } G = \left(\frac{GsRGB + 0.055}{1.055}\right)^{2.4} \tag{3}$$

$$\text{if } BsRGB \leq 0.03928 \text{ then } B = \frac{BsRGB}{12.92} \text{ else } B = \left(\frac{BsRGB + 0.055}{1.055}\right)^{2.4} \tag{4}$$

and RsRGB, GsRGB, and BsRGB are defined as:

$RsRGB = \frac{R8bit}{255}$, $GsRGB = \frac{G8bit}{255}$ and $BsRGB = \frac{B8bit}{255}$, respectively.

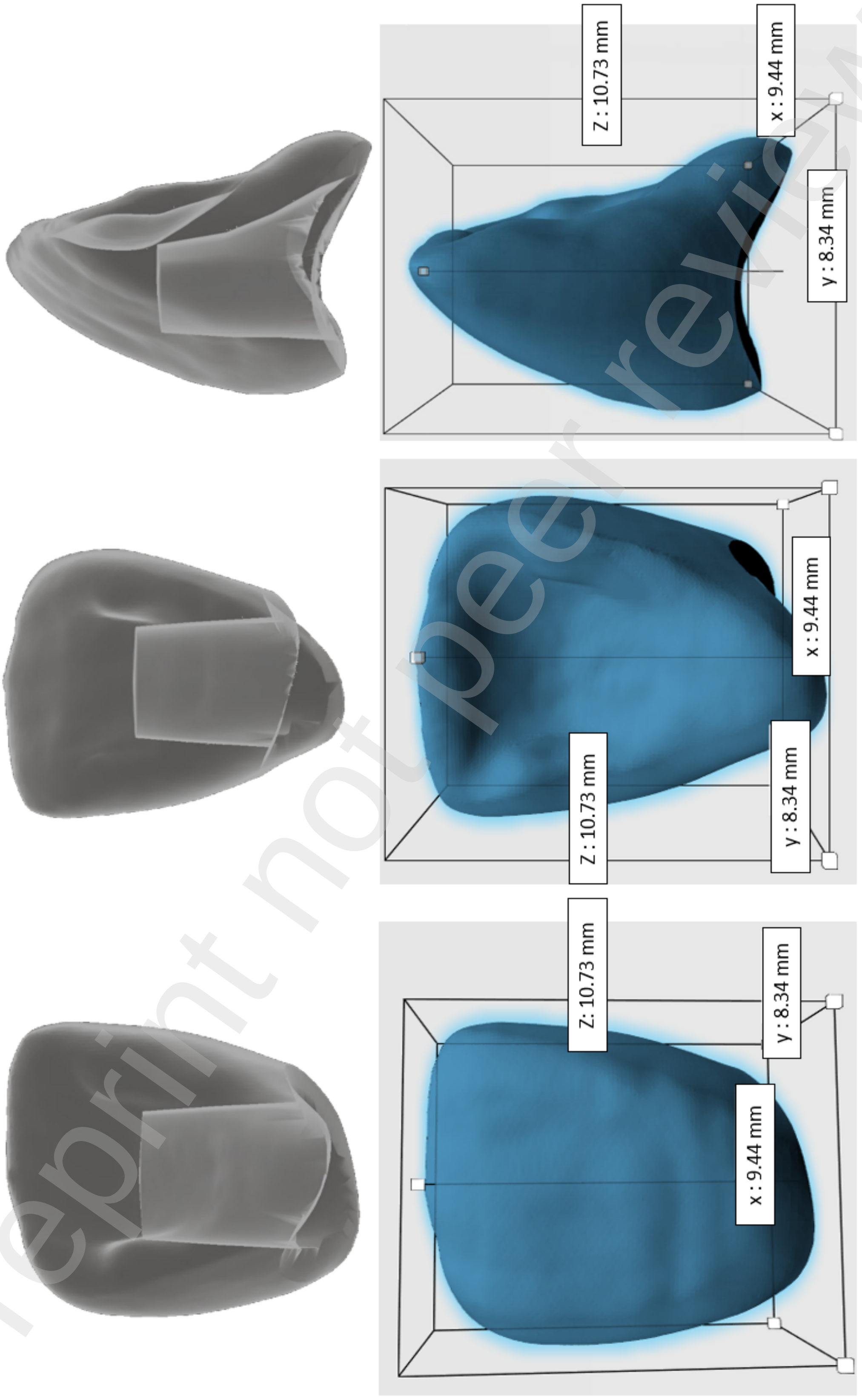

(a) Back view

(b) Front view

(c) Side view

Figure 4: Dimensions of the proposed dental crown model: (a) back view, (b) front view and (c) side view.

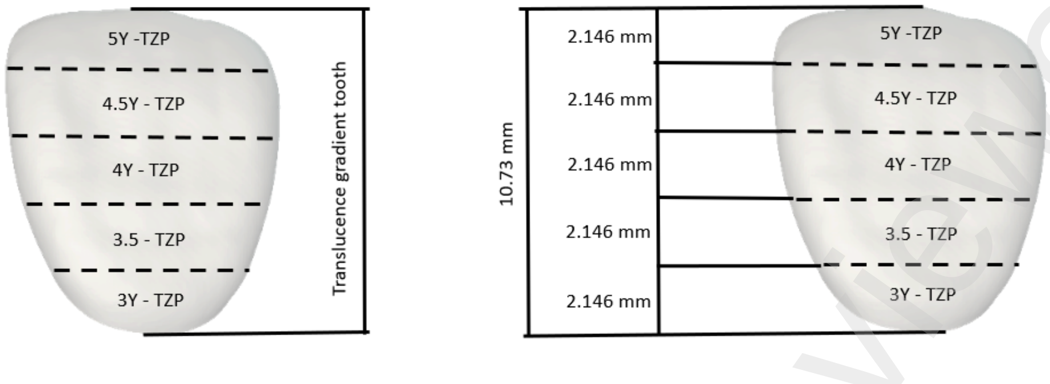

(a) (b)

Figure 5: Composition of the proposed dental crown model: (a) composition gradient tooth, (b) dimension gradient tooth.

3. Results and discussion

After the successful construction of the multi-slurry tape casting 3D printer, the printing performance is evaluated and the parameters were optimized to obtain high printing accuracy. The maximum solid loading is analyzed to determine the maximum amount of zirconia powder that can be added in the photocurable resin. Once the solid loading is determined, the depth of curing is evaluated at different exposure time. Apart from that, the temperature required for the sintering zirconia is identified. After successfully identifying the optimized parameters, the quality of the printed parts and cracks were evaluated. The shrinkage ratio, hardness, flexural, and translucency properties were analyzed.

3.1 Printable slurry with maximum solid loading – zirconia powder

The viscosity of a slurry is an important parameter that affects its printability and tape-casting performance. Figure 6 shows the viscosity of the slurries with different compositions of zirconia powder and resin combinations (i.e. zirconia/resin). Among the investigated compositions, the viscosity of the 80/20 composition was significantly higher than that of the other ratios. The increased viscosity is due to the higher percentage of solid particles in the slurry. As the solid content increases, particle interactions contribute to a thicker and more viscous slurry [30]. A higher proportion of powder in the slurry has advantages, such as increased strength of the green body and reduced shrinkage during the sintering process. [39].

The print quality of the green body was analyzed with 80% of zirconia powder. The print was found to be satisfactory without any defects. Moreover, when the % of zirconia was increased beyond 80%, it was found that the print quality was distorted due to difficulty in paving and scrapping. Thus, all further studies of parameters optimization were carried out with 80/20 zirconia-to-resin composition.

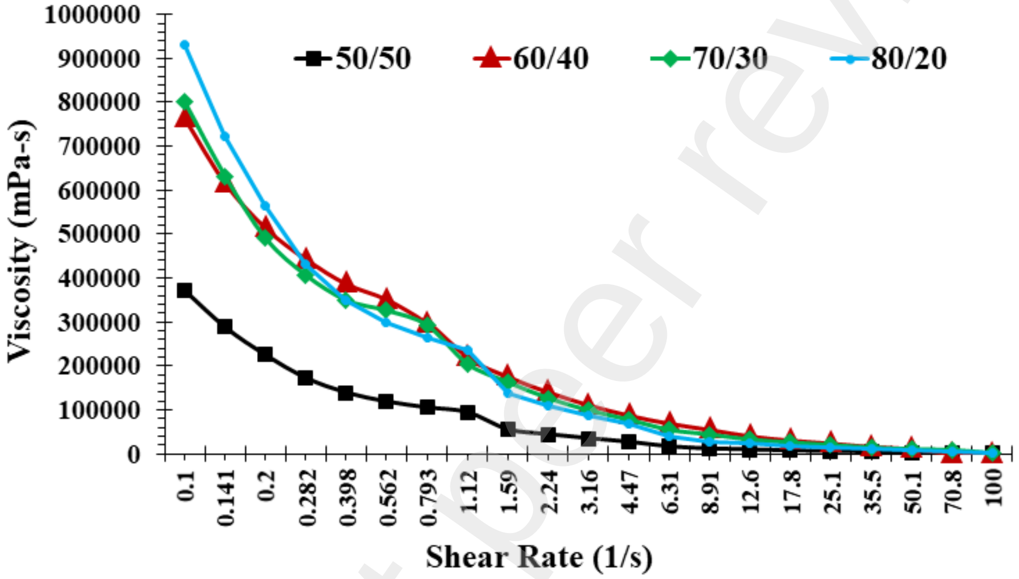

Figure 6: Viscosity of slurries with different compositions of zirconia powder and resin.

3.2 Curing depth vs Exposure Time

The objective of this study was to explore the influence of exposure time (ranging from 10 to 100 seconds) on the curing depth of the slurry compositions with different ratios of powder to resin components. The slurry compositions tested included 50/50, 60/40, 70/30, and 80/20. Figure 7 presents the relationship between curing depth and exposure time for different slurry compositions. It was observed that the curing depth increased with longer exposure times, a phenomenon that is consistent with the behavior of many photopolymerization processes. With the increase in the exposure time, the photo initiator had more time to react with the light source, thereby leading to a greater extent of solidification in the slurry.

In terms of slurry composition, the 50/50 (50% zirconia and 50% resin) slurry composition had the thickest depth of curing due to higher % of resin. With decrease in the resin concentration, the curing depth decreases. The increased powder content might have influenced the light penetration and energy absorption within the slurry, thus affecting curing depth [40].

Greater curing depth represents lesser printing time for a given design. Thus, with increase in zirconia concentration, printing quality increases at the expense of printing time. However, in the current study, more emphasis is given to the performance of printing ability (in terms of quality and porosity) of this newly developed 3D printer. Thus, 80/20 zirconia-to-resin composition is considered for the further studies.

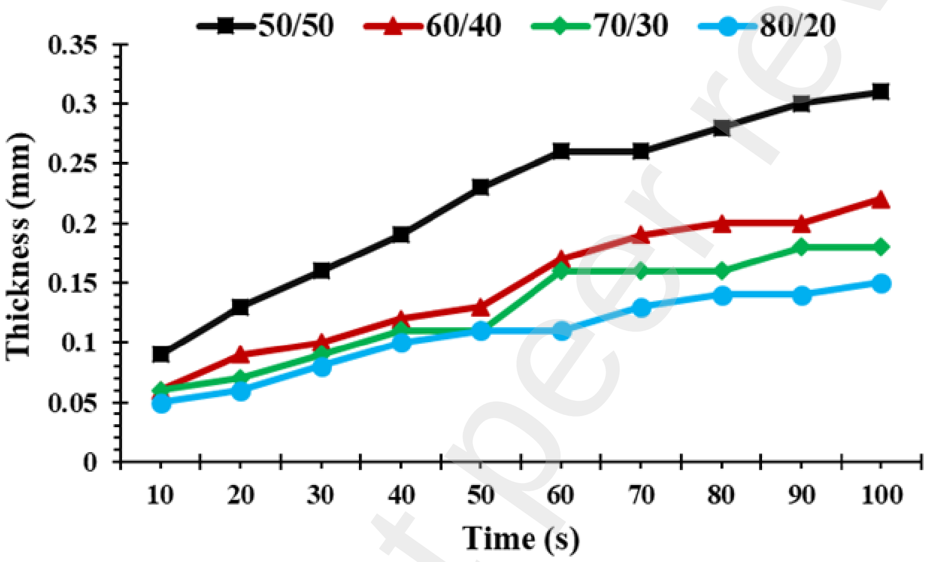

Figure 7: Cured layer thickness with different exposure time and compositions.

3.2 TGA versus two-step sintering parameter

The Thermogravimetric Analysis (TGA) illustrates the thermal behavior of the material, specifically its weight change as a function of temperature. Figure 8 demonstrates weight decrement at 300°C which indicates a significant change that occurs within the material. At 300°C, the material undergoes a debinding stage. During the debinding stage, the elevated temperature causes the binders to thermally degrade and evaporate.

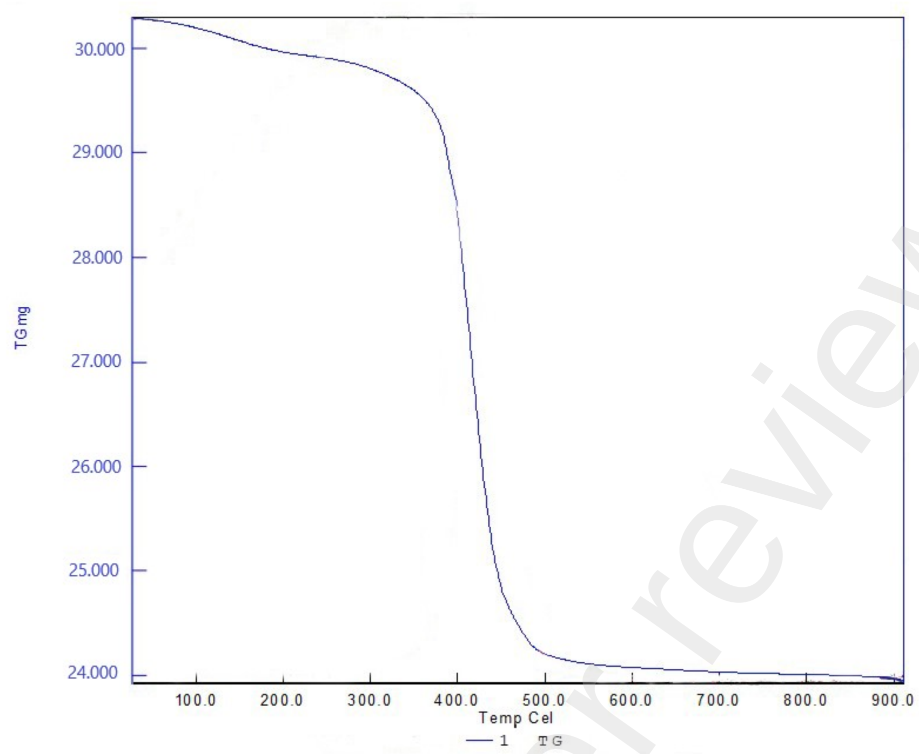

Figure 8: TGA result on zirconia slurry showing thermal degradation and evaporation of binder starting at 300ºC.

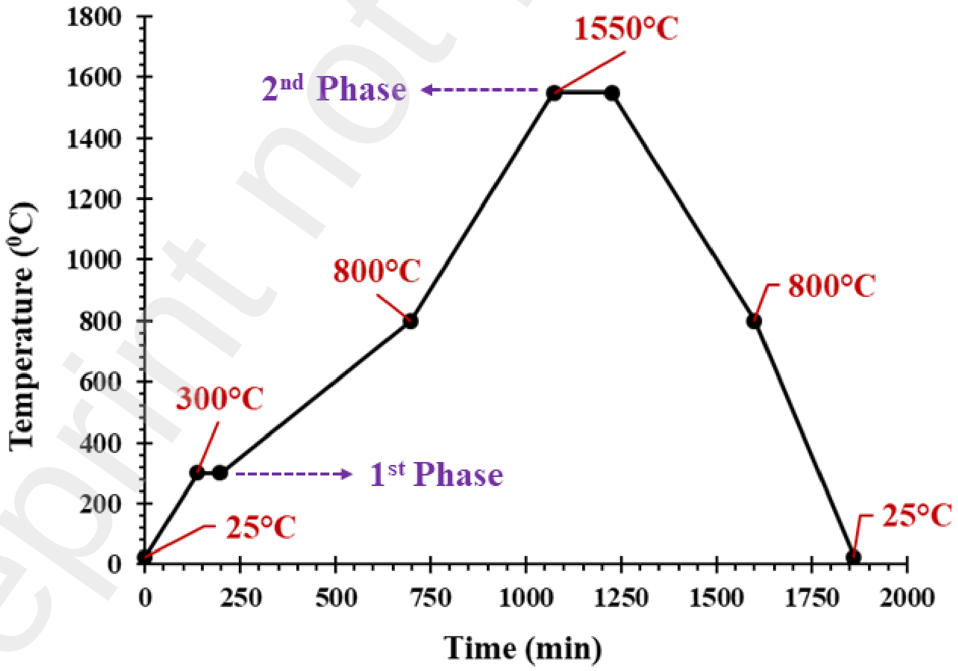

Figure 9: Two-phase sintering and their corresponding temperature of zirconia green body.

Two phase sintering process is followed in this study to achieve the desired structural and mechanical properties in the additively manufactured objects. Figure 9 shows the sintering temperature of zirconia with time. The initial stage involves gradually heating the material from room temperature to 300°C (based on the result obtained from Figure 8). In this step, any residual moisture or volatile components was cleaned from the green body. Once the temperature reaches 300°C, the green body is exposed to this temperature for 60 minutes. During this stage, it is ensured that the entire body is heated uniformly, thereby allowing comprehensive and consistent debinding.

The gradual increase of temperature from 300°C to 800°C shown in Figure 9 facilitates complete evaporation of the resin. The slow heating rate of 1°C/min is applied during debinding to reduce the risk of cracking caused by rapid resin evaporation. Sintering process begins as the temperature reaches 1550°C. The powder particles undergo diffusion-driven bonding to achieve higher density and improved mechanical properties at this temperature. The sample is held at this temperature for 1.5 hours to ensure uniform sintering without any defects or incomplete consolidation. The final cooling stage involves gradually reducing the temperature to room temperature as shown in Figure 9. This controlled cooling stage helps prevent thermal shock and ensures the stability of sample.

3.3 Post-sintering cracks in the fabricated samples

The microscopic images of the sintered samples with different zirconia and resin compositions are shown in Figure 10. Figure 10a shows that the higher percentage of resin (i.e. 50%) leads to loose packing of zirconia powder particles. This would eventually lead to generation of cracks upon sintering (Figure 10a). Such cracks may lead to failure of components under service and may compromise the performance. Figure 10 shows that with higher powder content, the density of cracks drastically decreases. With 70% powder content, the sample shows a small crack as shown in Figure 10c. As can be seen in Figure 10d, no cracks were generated when the powder content was increased to 80%. Thus, the quantity and compaction of powder particles was sufficient to prevent any crack upon sintering. It was further observed that increasing the powder content beyond 80% leads to improper cohesion between the powder particles, leading to failure of printing.

Thus, having thoroughly analyzed the sintered samples and considering the sintering behavior, crack formation, and overall printability, it becomes evident that the 80/20 composition stands out as the most promising choice for this zirconia 3D printing.

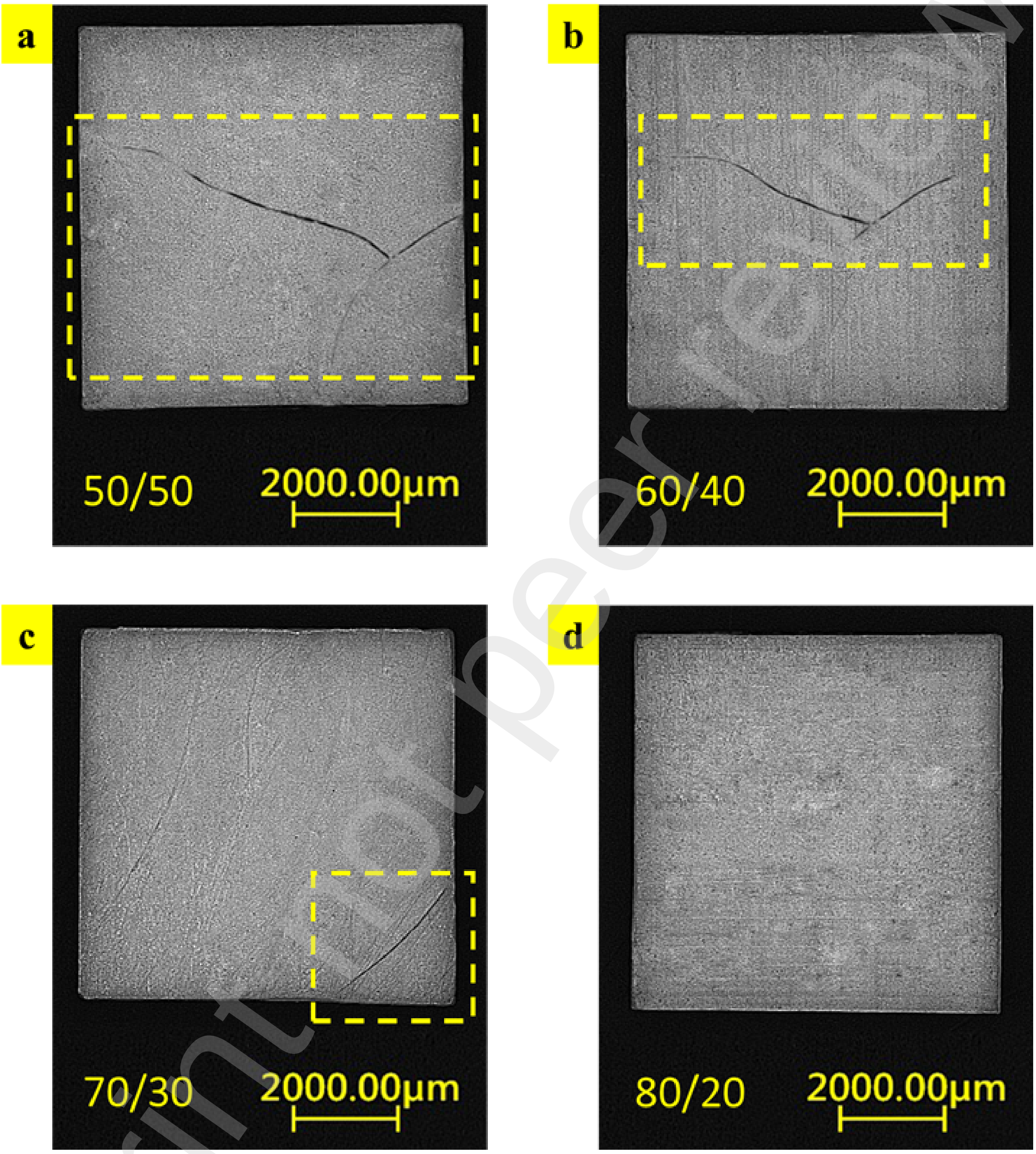

Figure 10: Microscopic images of post-sintered samples with different compositions of zirconia and resin.

Figure 11a. shows the SEM picture of the 80/20 composition. As the sintering temperature rises, the atoms across the surface of powder particles become gains higher energy state. This eventually leads to migrating and redistributing towards lower-energy state [41] . When the powder particles are compactly packed, these higher energy atoms can diffuse across the particle boundaries and accumulate in the new contact region. As the sintering progresses, the concentration of diffusing atoms at the particle interfaces grows, leading to the gradual formation of necks as shown in Figure 11b.

After several considerations, such as printability, surface morphology and the sintering behavior, the printing parameters for zirconia slurry are standardized as listed in Table 2.

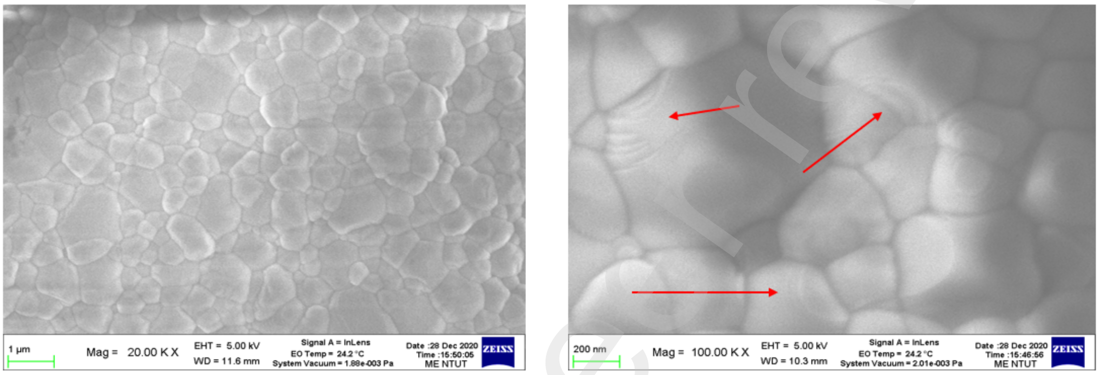

(a) (b)

Figure 11: SEM image of the sample printed with optimized composition (a) 80/20 zirconia/resin composition (b) necking phenomena due to diffusion of atoms.

Table 2: Printing parameter zirconia slurry

Parameter	Value
Weight ratio of zirconia powder to resin	80/20
Exposure time (s)	30
Layer thickness (µm)	50

3.6 Shrinkage ratio analysis

As mentioned in the previous sections of 3.1 and 3.2, the composition consisting of 80% zirconia and 20% resin is used to analyze the shrinkage ratio. Different mol.% of Y_2O_3 is added to zirconia to tune the mechanical and translucency properties. The five different types of zirconia powder: 3Y-TZP, 3.5Y-TZP, 4Y-TZP, 4.5Y-TZP, and 5Y-TZP are used as explained in section 2.2. The sample was designed with the dimension of 10 mm x 15 mm x 5 mm. Table 3 represented the dimensional changes in green bodies and sintered parts fabricated with different compositions of yttrium oxide.

The results of the investigation reveal that the shrinkage ratios for both the X and Y axes are approximately 20 ± 1% for all compositions of yttrium oxide (Table 3). These shrinkage ratios play a pivotal role in determining the scaling adjustments required in CAD designs. The shrinkage along the Z-axis was observed to be ~ 3% higher compared to that along X and Y axes. The higher % of shrinkage can be attributed to the printing direction along the Z-axis. When objects are printed layer by layer in the Z direction, the stacking of layers can lead to a cumulative effect on the overall shrinkage [42].

Thus, while designing the samples in CAD platform, the shrinkage allowance of 20%, 20%, and 23% must be given along the X, Y, and Z axes, respectively. This shrinkage allowance is further validated with different dimensions of the target bodies as shown in Figure 12. The shrinkage allowance of 20 x 20 x 23% was given to the two 3D models (CAD bodies) to reach their respective targeted dimension after sintering. It can be observed from Figure 12 that the % of error between the targeted dimension and the dimension of the actual sample is < 1% in both the samples. This consistency in dimensional accuracy signifies the reliability of the chosen shrinkage ratio.

Table 3: Dimension of the zirconia specimen before and after sintering

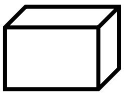 Dimension (w x d x h): 10mm x 15mm x 5mm		3Y-TZP	3.5Y-TZP	4Y-TZP	4.5Y-TZP	5Y-TZP
Green Body	X_{avg} (mm)	10.03	10.03	10.06	10.06	10.08
	Y_{avg} (mm)	15.03	15.03	15.05	15.03	15.06
	Z_{avg} (mm)	5.09	5.06	5.01	5.01	5.03
	Density $_{avg}$ (g/cm^3)	2.381	2.382	2.374	2.379	2.240
	Volume $_{avg}$ (cm^3)	0.783	0.785	0.780	0.780	0.784
	Weight $_{avg}$ (g)	1.865	1.870	1.852	1.855	1.756
Sintering Part	X_{avg} (mm)	8.03	7.99	7.99	7.95	7.99
	Y_{avg} (mm)	12.08	12.08	12.05	12.05	12.04
	Z_{avg} (mm)	3.90	3.92	3.86	3.88	3.88
	Density $_{avg}$ (g/cm^3)	5.883	5.846	5.860	5.860	5.848
	Volume $_{avg}$ (cm^3)	0.209	0.216	0.209	0.209	0.204
	Weight $_{avg}$ (g)	1.230	1.262	1.225	1.225	1.193
Shrinkage %	X_{avg} (%)	19.96%	20.30%	20.58%	20.99%	20.69%
	Y_{avg} (%)	19.64%	19.63%	19.97%	19.85%	20.03%
	Z_{avg} (%)	23.26%	22.60%	23.09%	22.69%	22.79%
Volume shrinkage $_{avg}$ (Vol.%)		49.36%	49.58%	48.88%	48.96%	48.97%
Weight Loss $_{avg}$ (wt. %)		34.05%	32.52%	33.84%	33.94%	32.07%

Targeted	3D model	Result
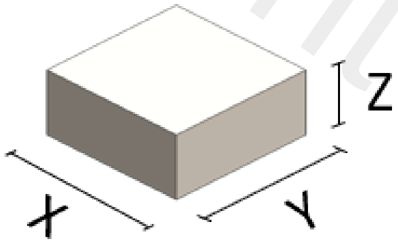	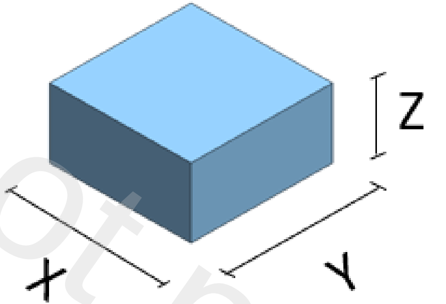	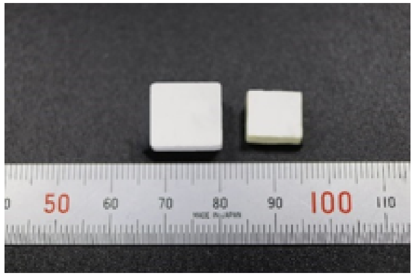
x : 10 mm y: 10 mm z: 5mm	x : 12 mm y: 12 mm z: 6.15mm	x : 10.09 mm y: 10.03 mm z: 4.95mm
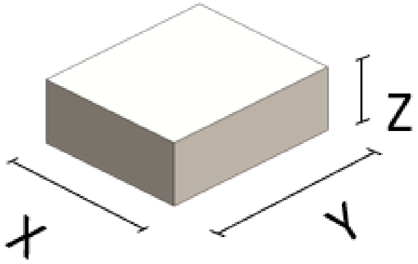	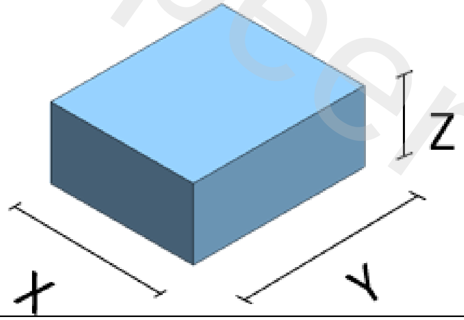	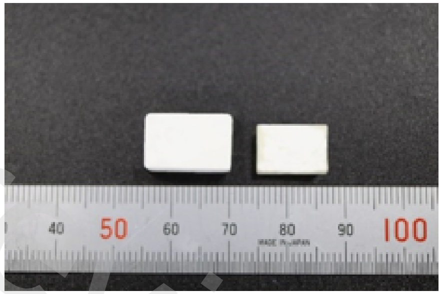
x : 12 mm y: 10 mm z: 5mm	x : 14.4 mm y: 12 mm z: 6.15mm	x : 12.08 mm y: 9.94 mm z: 5.05mm

Figure 12: Shrinkage allowance given to the 3D model (CAD design) to obtain the targeted dimensions in actual samples post sintering.

3.4 Mechanical properties and translucency

3.4.1 Hardness and flexural strength

Figure 13a illustrates the hardness of the 5 different compositions of yttrium oxide (Y_2O_3) in zirconia powder. Five specimens of each composition were used to determine the Vickers hardness values. The hardness value of each composition would help to evaluate the effect on yttrium oxide concentration on the hardness value of the specimens. As can be seen from Figure 13a, the Vickers hardness value decreases from the average value of 1687 HV to 1342 HV with the increase in composition of Y_2O_3 from 30% to 50%, respectively. This marks the reduction in hardness value by approximately 20% with the 20% increase in Y_2O_3 composition. The graph in Figure 13a illustrates a slight decrease of approximately 20% in hardness across the different zirconia compositions, from 3Y to 5Y. This trend observed in Figure 13a corresponds to the relationship between yttrium oxide concentration and the stability of the tetragonal and cubic phases in zirconia. As yttrium oxide content increases, the tetragonal phase becomes more dominant due to the stabilizing effect of yttrium ions. This shift in phase composition affects the mechanical properties, with the tetragonal phase being associated with lower hardness [43].

Figure 13b shows the variation in flexural strength of the specimens with different zirconia powders. The data reveals that the average flexural strength for the 3Y-TZP is around 650.61 MPa, which is the highest value observed in the 3Y zirconia. This result is consistent with the prior discussion on the influence of yttrium oxide content on material strength. The lower yttrium oxide concentration in 3Y zirconia promotes the tetragonal phase, leading to greater transformation toughening effects and enhanced resistance to crack propagation [44, 45]. The lowest flexural strength in the 5Y-TZP zirconia composition, the average measuring around 409.02 MPa. This result is attributed to the higher concentration of the cubic phase in the 5Y-TZP zirconia due to lower yttrium content. The absence of substantial transformation toughening mechanisms in the cubic phase contributes to reduced flexural strength and overall material toughness.

The results in Figure 13 demonstrates that 3Y-TZP with lower yttrium content, exhibit superior hardness and flexural strength compared to other kind of zirconia powders containing higher yttrium concentrations. Higher yttrium concentrations favor the presence of the cubic phase.

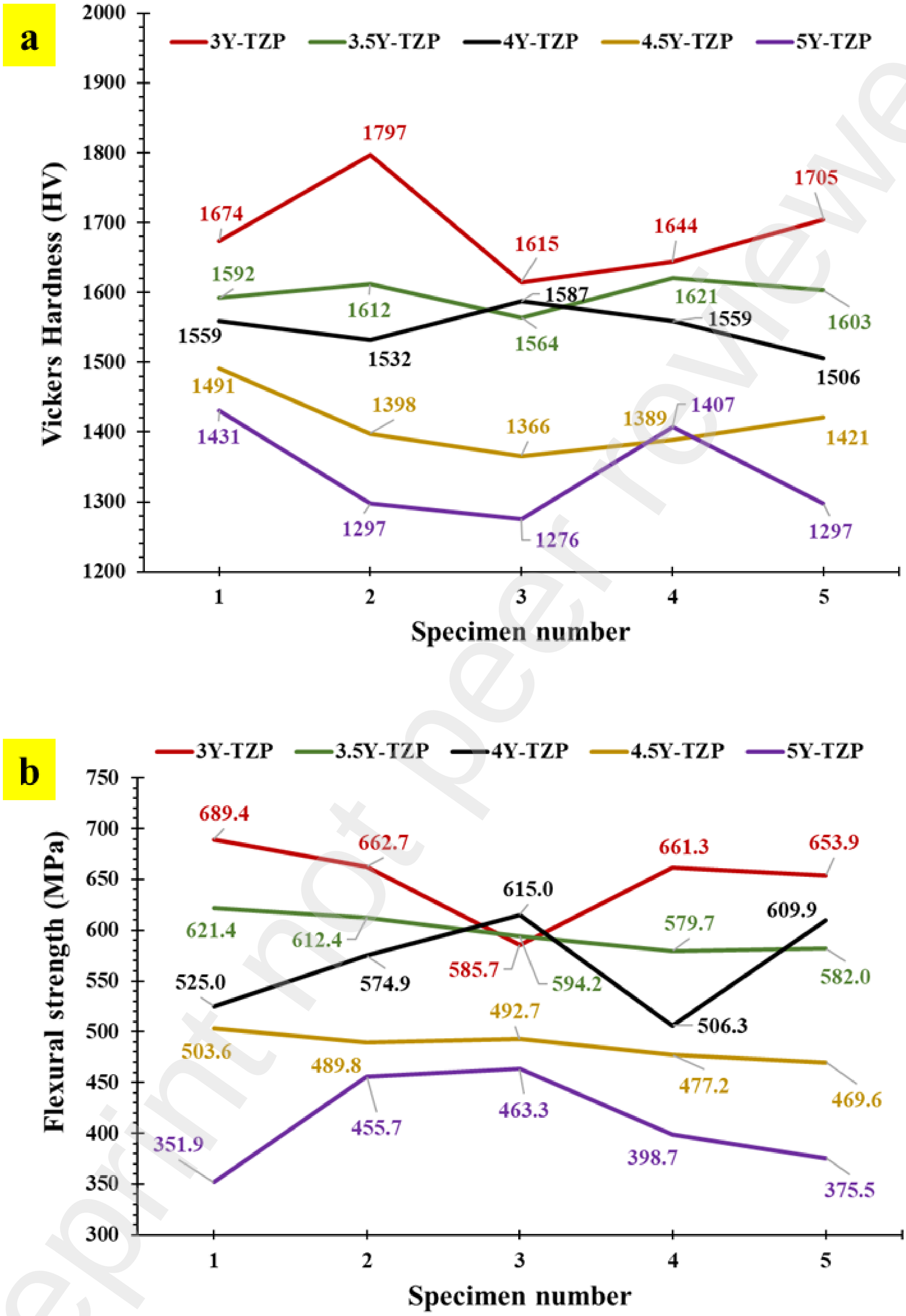

Figure 13: Mechanical properties of specimens with different Y_2O_3 and zirconia powder composition: a) Vickers hardness and b) flexural strength.

3.4.2 Translucency

The translucency of the printed specimen was tested as shown in Figure 14. The specimen of thickness 2 mm and diameter 10 mm was placed over an LED light (Figure 14a). The translucency of the specimens is tested at 5 different points in terms of their RGB value (Red, Green, and Blue) as shown in Figure 14b.

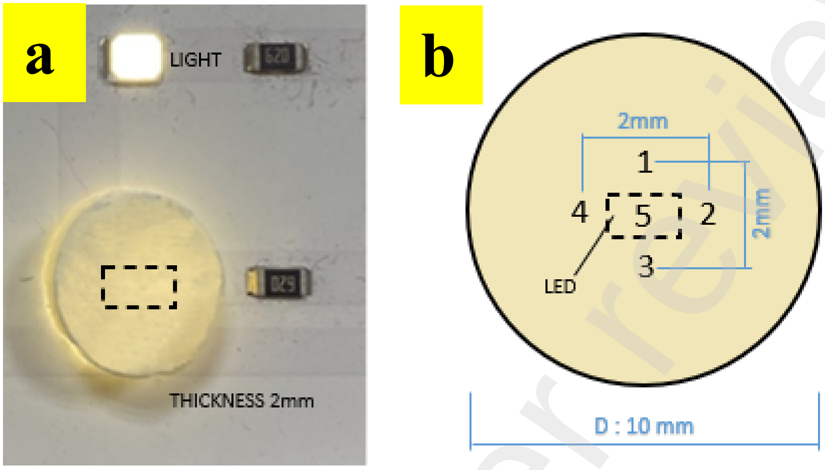

Figure 14: Relative luminance test (a) single material translucency test (b) points to test.

In this research, the RGB value is tested at each point, the average of the 5 points will be calculated as the relative luminance value. Table 4 shows the RGB value of each sample with different yttrium oxide concentration. The relative luminance is calculated using the Equation 1 explained in section 2.8.1.

Table 4: The relative luminance of single material test value

Single Material				
Sample	**$R_{\text{8bit (avg)}}$**	**$G_{\text{8bit (avg)}}$**	**$B_{\text{8bit (avg)}}$**	**Relative Luminance**
3Y-TZP	236.00	222.00	173.40	73.12%
3.5Y-TZP	241.40	227.40	177.40	77.12%
4Y-TZP	241.80	229.60	176.20	78.36%
4.5Y-TZP	244.60	230.40	182.00	79.53%
5Y-TZP	248.60	234.40	184.20	82.61%

Table 4 shows the results of a single test on 3Y-TZP,3.5-TZP, 4Y-TZP, 4.5Y-TZP and 5Y-TZP materials, it can be seen that 5Y (82.61%) has the highest relative luminance and 3Y-TZP (73.12%) is the lowest relative luminance.

Similar experiment is also performed on the cuboid samples. Figure 15 shows a sample with thickness 1mm manufactured with multi-slurry tape casting 3D printer. In the sample, it can be seen that there is a clear gradation of zirconia in 3Y-TZP, 3.5Y-TZP, 4Y-TZP, 4.5Y-TZP, and 5Y-TZP. The most translucent zirconia material is 5Y-TZP, followed by 4.5Y-TZP, 4Y-TZP, 3.5Y-TZP and then 3Y. This is due to the difference in material composition between them. The alumina composition contained in 3Y zirconia is generally 0.25 wt.%, limiting their translucency [46].

The cubic phase content of zirconia increases as the Y_2O_3 (yttrium oxide) content increases [47]. More light will be transmitted due to the increasing volume of the cubic phase and the isotropic properties of this cubic phase will make the material appear more translucent [48].

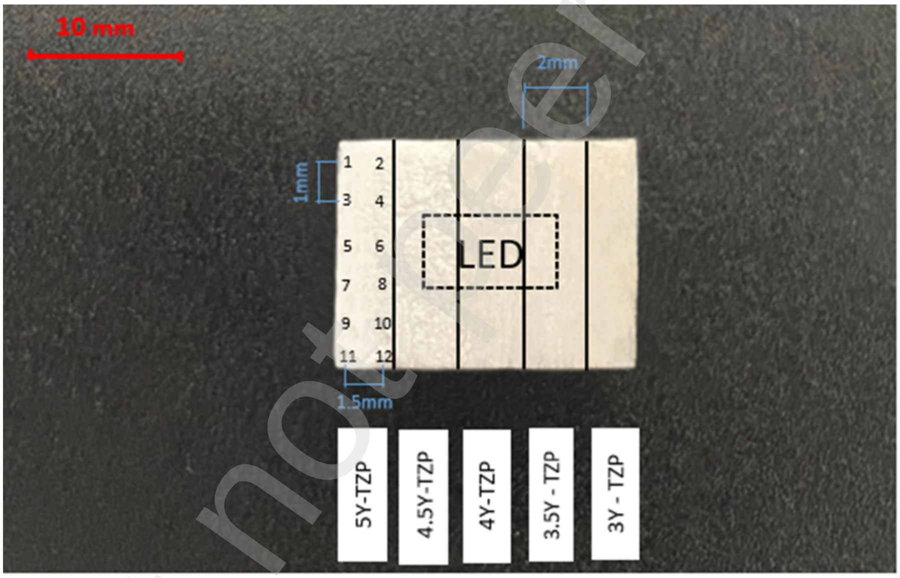

Figure 15: Gradient material of zirconia

Table 5 shows the value of the relative luminance of each color element: red (R_{8bit}), green (G_{8bit}), and blue (B_{8bit}). 12 points were taken to find out the average value of each section based on relative luminance calculations [38].

Table 5: The relative luminance of gradient material test value

Gradient Material				
Sample	**$R_{8bit\ (avg)}$**	**$G_{8bit\ (avg)}$**	**$B_{8bit\ (avg)}$**	**Relative Luminance**
3Y-TZP	231.92	221.50	193.83	73.01%
3.5Y-TZP	233.92	224.17	201.58	75.12%
4Y-TZP	234.92	227.33	210.75	77.46%
4.5Y-TZP	236.83	228.75	208.67	78.46%
5Y-TZP	236.83	231.50	217.58	80.45%

3.5 Post-Processing and application in dental crown

3D printed parts often require post-processing to improve surface finish, reduce imperfections, and make aesthetically pleasing. In this study, the fabricated samples are surface polished to remove layer lines. Such polishing of green body before sintering is essential to reduce friction, wear, and the accumulation of debris. Furthermore, polishing allows for the fine-tuning of dimensions and tolerances. During additive manufacturing, slight variations in layer deposition can lead to change in dimensions. By smoothing out surface irregularities, minimizing layer lines, and eliminating imperfections, the resulting tooth model closely mimics natural teeth. The significance of surface polishing is shown in Figure 16.

The potential of this technology can be harnessed in the various biomedical equipment and dental crown. Figure 17 shows the dental crown model which exactly mimics the actual dental crown. Fabrication of such implants using traditional techniques is challenging due to the requirement of customization. As the size and color (appearance) of teeth set is different in each person, the dental crown have to be carefully fabricated to resemble rest of the teeth. During the additive manufacturing technique using multi-slurry tape casting, the color and size of the tooth can be easily varied and fabricated in a single step. The results indicate that the bonding between layers satisfies the requirements, with no evidence of cracks or deformation.

Moreover, Figure 18 depicts the gradient translucency of tooth with varying % of yttrium concentration to control and manipulate the appearance (essential for customized mimicking of dental crown). This gradient pattern is strategically designed to mimic the natural gradient of a tooth, from its dentin-like base to its more translucent incisal region. Higher yttrium concentrations tend to stabilize the cubic phase, which possesses superior translucence compared to the tetragonal phase. As the yttrium content increases, the cubic phase becomes more dominant, thus enhancing the translucence of material [49]. This aligns with the observed gradient translucence in the Figure 18.

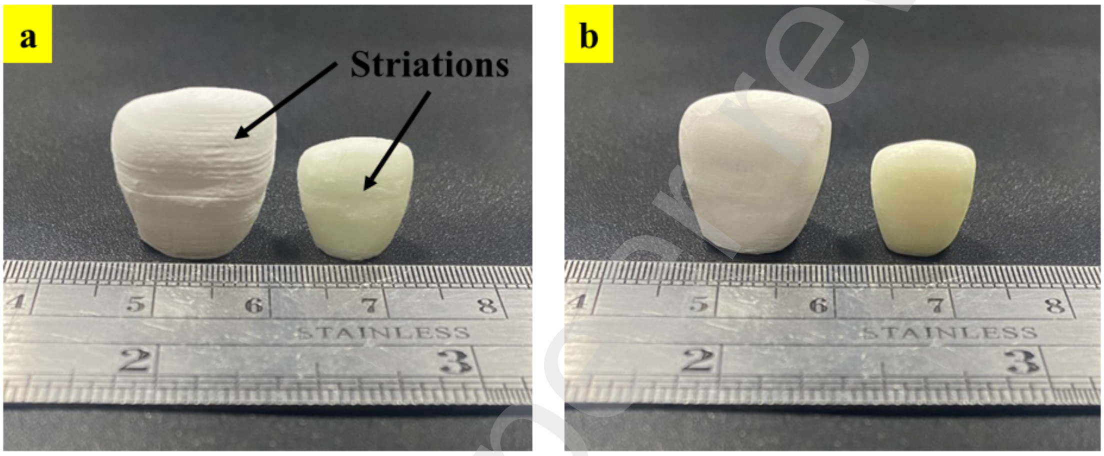

Figure 16: The benchmark dental crownmodel: (a) without post processing (b) with processing.

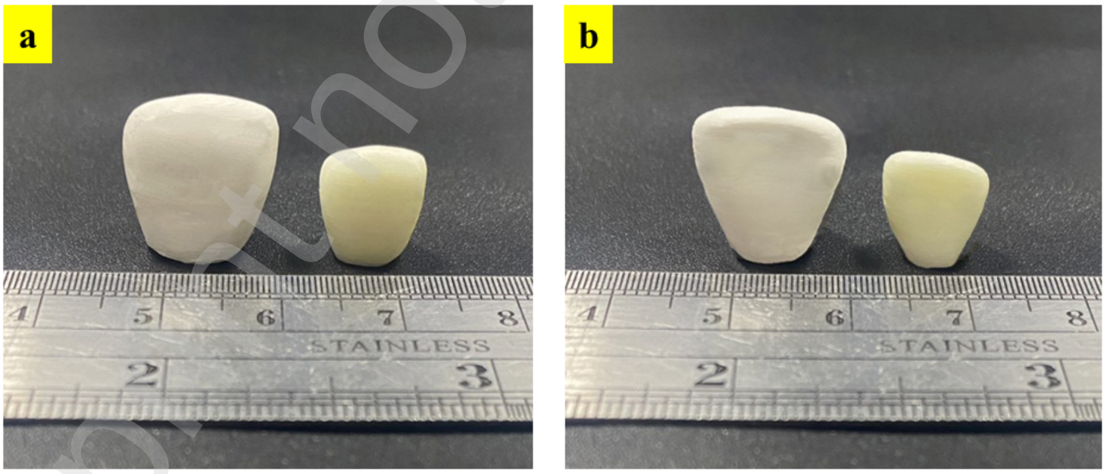

Figure 17: The dental crown model: (a) back view (b) front view.

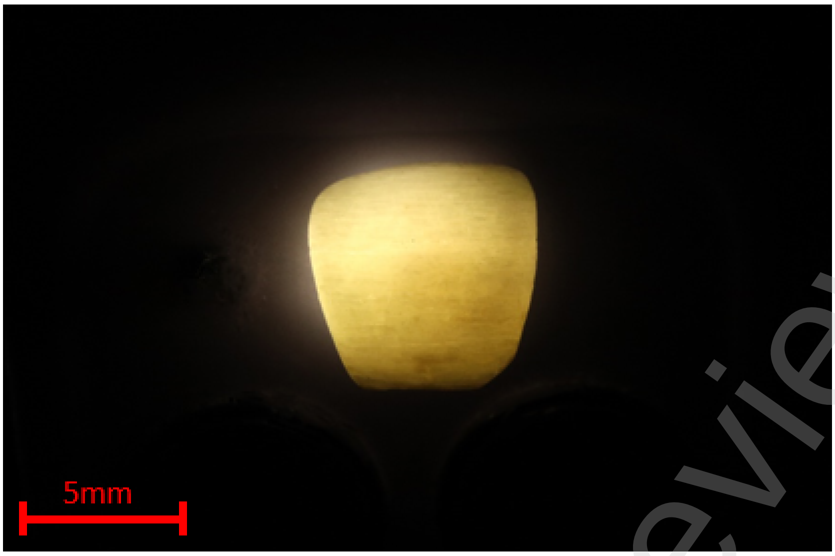

Figure 18: The dental crown model mimicking the appearance of actual tooth with gradient translucency.

4. Conclusion

The fabrication of functionally graded materials has always been challenging using both tradition and additive manufacturing techniques. Owning to their exception ability of tuning mechanical and functional properties, these materials are of high demand in various locomotive and biomedical industries.

In this comprehensive research, a novel multi-slurry tape casting 3D printing technology is proposed for the fabrication of FGMs in a single stage. The 3D printer was indigenously developed based on the proposed technique and demonstrated its working performance. The developed 3D printer performed well with acceptable accuracy and consistency in fabricating zirconia based FGMs. Through meticulous analysis, the optimal composition of 80/20 in terms of zirconia powder and resin ratio is identified as the best composition. This composition showcased favorable viscosity characteristics for effective slurry application and printing. Moreover, the samples printed with this composition did not show any surface cracks upon sintering. The shrinkage analysis determined the necessary shrinkage allowance of 20%, 20%, and 23% in CAD models along X, Y, and Z directions, respectively. After successful optimization of printing parameters, the samples were fabricated with different proportions of zirconia-yttria compositions. The optimized composition of zirconia/yttria was found to be 97/3 to obtain excellent hardness and flexural strength.

The maximum hardness of 1687 HV and flexural strength of 650.6 MPa was obtained at this composition. Adding yttrium oxide beyond 3% decreased the mechanical performance of the FGM. However, higher yttrium oxide increased the relative luminescence with highest luminescence of 81% at 5%. Such properties favor in the customization of dental crown based on the size and appearance of other teeth. The composition of yttrium can be easily manipulated and fabricated using the proposed technique.

Funding

This research was funded by National Science and Technology Council (NSTC) of Taiwan, grant number 111-2622-E-027 -028, 111-2221-E-027 -087 -MY2 and 112-2218-E-A49 -028.This work is also supported by the “High-value Biomaterials Research and Commercialization Center” of the Featured Area Research Center Program within the framework of the Higher Education Sprout Project by the Taiwan Ministry of Education (MOE).

Competing interests

The authors declare no competing interests.

Contributions

Conceptualization, Cho-Pei Jiang and Zhangwei Chen.; methodology, Cho-Pei Jiang; software, Yulius Shan Romario; validation Yulius Shan Romario and Chinmai Bhat ; investigation, Yulius Shan Romario and Chinmai Bhat; data curation, Yulius Shan Romario, Chinmai Bhat, Tim Pasang and Maziar Ramezani; writing—original draft preparation, Yulius Shan Romario and Chinmai Bhat ; writing—review and editing, Cho-Pei Jiang, Zhangwei Chen ,Maziar Ramezani and Tim Pasang; supervision, Cho-Pei Jiang.; project administration, Cho-Pei Jiang.; funding acquisition, Cho-Pei Jiang. All authors have read and agreed to the published version of the manuscript.

Reference

[1] A. Verma, A. Kapil, D. Klobčar, and A. Sharma, "A Review on Multiplicity in Multi-Material Additive Manufacturing: Process, Capability, Scale, and Structure," *Materials,* vol. 16, no. 15, p. 5246, 2023.

[2] C. Bhat, A. Kumar, S.-C. Lin, and J.-Y. Jeng, "A novel bioinspired architectured materials with interlocking designs based on tessellation," *Additive Manufacturing,* vol. 58, p. 103052, 2022.

[3] C. Bhat, A. Kumar, S.-C. Lin, and J.-Y. Jeng, "Adaptive mechanical properties and stretchability of novel chainmail fabrics based on overlapping tessellation strategies," *Additive Manufacturing,* vol. 76, p. 103777, 2023.

[4] M. Naebe and K. Shirvanimoghaddam, "Functionally graded materials: A review of fabrication and properties," *Applied materials today,* vol. 5, pp. 223-245, 2016.

[5] I. M. El-Galy, B. I. Saleh, and M. H. Ahmed, "Functionally graded materials classifications and development trends from industrial point of view," *SN Applied Sciences,* vol. 1, pp. 1-23, 2019.

[6] R. Ghanavati and H. Naffakh-Moosavy, "Additive manufacturing of functionally graded metallic materials: A review of experimental and numerical studies," *Journal of Materials Research and Technology,* vol. 13, pp. 1628-1664, 2021.

[7] V. Birman and L. W. Byrd, "Modeling and analysis of functionally graded materials and structures," 2007.

[8] V. Boggarapu, R. Gujjala, S. Ojha, S. Acharya, S. Chowdary, and D. kumar Gara, "State of the art in functionally graded materials," *Composite Structures,* vol. 262, p. 113596, 2021.

[9] B. Saleh *et al.*, "30 Years of functionally graded materials: An overview of manufacturing methods, Applications and Future Challenges," *Composites Part B: Engineering,* vol. 201, p. 108376, 2020.

[10] A. Pasha and B. Rajaprakash, "Functionally graded materials (FGM) fabrication and its potential challenges & applications," *Materials Today: Proceedings,* vol. 52, pp. 413-418, 2022.

[11] B. Saleh, J. Jiang, A. Ma, D. Song, D. Yang, and Q. Xu, "Review on the influence of different reinforcements on the microstructure and wear behavior of functionally graded aluminum matrix composites by centrifugal casting," *Metals and Materials International,* vol. 26, pp. 933-960, 2020.

[12] H. Tsukamoto, "Cyclic Thermal Shock Response of Zirconia/304 Stainless Steel Functionally Graded Materials Fabricated by Centrifugal Slurry Methods," *Journal of Composites Science,* vol. 7, no. 2, p. 69, 2023.

[13] Q. Wang, J. Shi, L. Zhang, S. Tsutsumi, J. Feng, and N. Ma, "Impacts of laser cladding residual stress and material properties of functionally graded layers on titanium alloy sheet," *Additive Manufacturing,* vol. 35, p. 101303, 2020.

[14] L. Dobrzański, L. Żukowska, J. Mikuła, K. Gołombek, D. Pakuła, and M. Pancielejko, "Structure and mechanical properties of gradient PVD coatings," *Journal of Materials Processing Technology,* vol. 201, no. 1-3, pp. 310-314, 2008.

[15] S. Heuer *et al.*, "Atmospheric plasma spraying of functionally graded steel/tungsten layers for the first wall of future fusion reactors," *Surface and*

coatings technology, vol. 366, pp. 170-178, 2019.

[16] B. Kieback, A. Neubrand, and H. Riedel, "Processing techniques for functionally graded materials," *Materials Science and Engineering: A,* vol. 362, no. 1-2, pp. 81-106, 2003.

[17] C. Bhat, A. Kumar, S.-C. Lin, and J.-Y. Jeng, "Design, fabrication, and properties evaluation of novel nested lattice structures," *Additive Manufacturing,* vol. 68, p. 103510, 2023.

[18] C. Zhang *et al.*, "Additive manufacturing of functionally graded materials: A review," *Materials Science and Engineering: A,* vol. 764, p. 138209, 2019.

[19] Y. Li *et al.*, "A review on functionally graded materials and structures via additive manufacturing: from multi-scale design to versatile functional properties," *Advanced Materials Technologies,* vol. 5, no. 6, p. 1900981, 2020.

[20] A. Reichardt *et al.*, "Advances in additive manufacturing of metal-based functionally graded materials," *International Materials Reviews,* vol. 66, no. 1, pp. 1-29, 2021.

[21] G. H. Loh, E. Pei, D. Harrison, and M. D. Monzón, "An overview of functionally graded additive manufacturing," *Additive Manufacturing,* vol. 23, pp. 34-44, 2018.

[22] M. Rafiee, R. D. Farahani, and D. Therriault, "Multi-material 3D and 4D printing: a survey," *Advanced Science,* vol. 7, no. 12, p. 1902307, 2020.

[23] M. C. Leu, B. K. Deuser, L. Tang, R. G. Landers, G. E. Hilmas, and J. L. Watts, "Freeze-form extrusion fabrication of functionally graded materials," *CIRP annals,* vol. 61, no. 1, pp. 223-226, 2012.

[24] S. Spiller, F. Berto, and N. Razavi, "Mechanical behavior of Material Extrusion Additive Manufactured components: an overview," *Procedia Structural Integrity,* vol. 41, pp. 158-174, 2022.

[25] S. Nohut, S. Geier, I. Kraleva, M. Schwentenwein, and R. Bermejo, "Lithography-based additive manufacturing of porosity graded alumina," *Additive Manufacturing Letters,* vol. 3, p. 100060, 2022.

[26] S. Nohut and M. Schwentenwein, "Vat photopolymerization additive manufacturing of functionally graded materials: a review," *Journal of Manufacturing and Materials Processing,* vol. 6, no. 1, p. 17, 2022.

[27] S. Weingarten *et al.*, "Multi-material ceramic-based components–additive manufacturing of black-and-white zirconia components by thermoplastic 3D-printing (CerAM-T3DP)," *JoVE (Journal of Visualized Experiments),* no. 143, p. e57538, 2019.

[28] L. Ren, Z. Wang, L. Ren, Z. Han, Q. Liu, and Z. Song, "Graded biological materials and additive manufacturing technologies for producing bioinspired graded materials: An overview," *Composites Part B: Engineering,* vol. 242, p. 110086, 2022.

[29] S. Hasanov *et al.*, "Review on additive manufacturing of multi-material parts: Progress and challenges," *Journal of Manufacturing and Materials Processing,* vol. 6, no. 1, p. 4, 2021.

[30] C.-P. Jiang, Y. S. Romario, and E. Toyserkani, "Development of a Novel Tape-Casting Multi-Slurry 3D Printing Technology to Fabricate the Ceramic/Metal Part," *Materials,* vol. 16, no. 2, p. 585, 2023.

[31] S. Zhang, I. A. Sutejo, J. Kim, Y. J. Choi, H. Park, and H. s. Yun, "Three-dimensional complex construct fabrication of illite by digital light processing-based additive manufacturing technology," *Journal of the*

American Ceramic Society, vol. 105, no. 6, pp. 3827-3837, 2022.

[32] A. Rosenberger, N. Ku, L. Vargas-Gonzalez, M. Alazzawi, and R. Haber, "Rheology and processing of UV-curable textured alumina inks for additive manufacturing," *International Journal of Applied Ceramic Technology,* vol. 18, no. 5, pp. 1457-1465, 2021.

[33] H. Xing, B. Zou, X. Liu, X. Wang, C. Huang, and Y. Hu, "Fabrication strategy of complicated Al2O3-Si3N4 functionally graded materials by stereolithography 3D printing," *Journal of the European Ceramic Society,* vol. 40, no. 15, pp. 5797-5809, 2020.

[34] G. Wang, S. Wang, X. Dong, Y. Zhang, and W. Shen, "Recent progress in additive manufacturing of ceramic dental restorations," *Journal of Materials Research and Technology,* 2023.

[35] H. Li, L. Song, J. Sun, J. Ma, and Z. Shen, "Dental ceramic prostheses by stereolithography-based additive manufacturing: potentials and challenges," *Advances in Applied Ceramics,* vol. 118, no. 1-2, pp. 30-36, 2019.

[36] L. Wang, H. Yu, Z. Hao, W. Tang, and R. Dou, "Fabrication of highly translucent yttria-stabilized zirconia ceramics using stereolithography-based additive manufacturing," *Ceramics International,* vol. 49, no. 11, pp. 17174-17184, 2023.

[37] B. Stawarczyk, M. Özcan, L. Hallmann, A. Ender, A. Mehl, and C. H. Hämmerlet, "The effect of zirconia sintering temperature on flexural strength, grain size, and contrast ratio," *Clinical oral investigations,* vol. 17, pp. 269-274, 2013.

[38] B. Caldwell *et al.*, "Web content accessibility guidelines (WCAG) 2.0," *WWW Consortium (W3C),* vol. 290, pp. 1-34, 2008.

[39] A. Mukherjee, B. Maiti, A. D. Sharma, R. N. Basu, and H. S. Maiti, "Correlation between slurry rheology, green density and sintered density of tape cast yttria stabilised zirconia," *Ceramics International,* vol. 27, no. 7, pp. 731-739, 2001.

[40] S. P. Gentry and J. W. Halloran, "Light scattering in absorbing ceramic suspensions: Effect on the width and depth of photopolymerized features," *Journal of the European Ceramic Society,* vol. 35, no. 6, pp. 1895-1904, 2015.

[41] S. Ji, Z. Liu, G. Wang, Y. Liu, and Y. Jing, "Effects of sintering temperature and particle size on permeability of functionally gradient composite porous materials prepared by hanging slurry process," *SN Applied Sciences,* vol. 2, pp. 1-20, 2020.

[42] B. Coppola, J. Schmitt, T. Lacondemine, C. Tardivat, L. Montanaro, and P. Palmero, "Digital light processing stereolithography of zirconia ceramics: Slurry elaboration and orientation-reliant mechanical properties," *Journal of the European Ceramic Society,* vol. 42, no. 6, pp. 2974-2982, 2022.

[43] V. V. Rodaev, S. S. Razlivalova, A. I. Tyurin, A. O. Zhigachev, and Y. I. Golovin, "Microstructure and phase composition of yttria-stabilized zirconia nanofibers prepared by high-temperature calcination of electrospun zirconium acetylacetonate/yttrium nitrate/polyacrylonitrile fibers," *Fibers,* vol. 7, no. 10, p. 82, 2019.

[44] V. Kulyk, Z. Duriagina, A. Kostryzhev, B. Vasyliv, V. Vavrukh, and O. Marenych, "The effect of yttria content on microstructure, strength, and fracture behavior of yttria-stabilized zirconia," *Materials,* vol. 15, no. 15, p. 5212, 2022.

[45] A. M. Arellano Moncayo, L. Peñate, M. Arregui, L. Giner-Tarrida, and R.

Cedeño, "State of the art of different zirconia materials and their indications according to evidence-based clinical performance: A narrative review," *Dentistry Journal,* vol. 11, no. 1, p. 18, 2023.

[46] F. Zhang *et al.*, "Strength, toughness and aging stability of highly-translucent Y-TZP ceramics for dental restorations," *Dental Materials,* vol. 32, no. 12, pp. e327-e337, 2016.

[47] B. Stawarczyk, C. Keul, M. Eichberger, D. Figge, D. Edelhoff, and N. Lümkemann, "Three generations of zirconia: From veneered to monolithic. Part I," *Quintessence international,* vol. 48, no. 5, 2017.

[48] Y.-M. Chen, R. J. Smales, K. H.-K. Yip, and W.-J. Sung, "Translucency and biaxial flexural strength of four ceramic core materials," *Dental Materials,* vol. 24, no. 11, pp. 1506-1511, 2008.

[49] S. Kongkiatkamon, D. Rokaya, S. Kengtanyakich, and C. Peampring, "Current classification of zirconia in dentistry: an updated review," *PeerJ,* vol. 11, p. e15669, 2023.